Methodology to Predict Stiffness Knock-down in Laminates for Wind Turbine Blades with Artificial Wrinkles

Heloisa Guedes Mendonça[1,2], Lars Pilgaard Mikkelsen[1], Xiao Chen[1], Johannes Bode[2], Flemming Mortensen[2], Philipp Ulrich Haselbach[1], and Kim Branner[1]

[1]Department of Wind Energy, Technical University of Denmark, Frederiksborgvej 399, 4000 Roskilde, Denmark
[2]Vestas Wind Systems, Hedeager 42, 8200 Aarhus , Denmark

Correspondence: Heloisa Guedes Mendonça (hegmen@dtu.dk)

Abstract. This work presents a methodology to evaluate the effect of wrinkles defects in the stiffness response of laminates characteristic of wind turbine blades. The assessment is carried out through numerical models and experimental tests with coupon specimens embedded with artificial wrinkles. Specimens are manufactured with two types of defects, prone to arise along the manufacturing process of wind turbine blades. Image-based numerical models were built to enclose the actual features of the cross-sectional wrinkling of each defect type. Experimental quasi-static tension and compression tests were performed, where extensometers collect the strain distribution about the wrinkle section as around the flat section of the test specimens. 2D finite element simulations carried out in Abaqus/Standard captured the stiffness behaviour of the two types of wrinkles. The numerical approach is validated against the quasi-static tests retrieving a fair agreement with experimental data. A significant knock-down in the stiffness response was found due to the wrinkle with larger aspect ratio amplitude/half-wavelength.

1 Introduction

Wrinkles are manufacturing induced defects, which can impact the production cycle time leading to expensive repairs when required, ultimately resulting in a decline of wind turbine blades reliability. This study is dedicated to evaluate out-of-plane wrinkles due to its critical impact on the structural performance of the blade. Thus, the term wrinkles in this study are interpreted as out-of-plane wrinkles. Out-of-plane wrinkles is a result of fibre bending out of the laminate and layer bending through-thickness (Wang, L. (2001), Lightfoot, et al. (2013)). On the other hand, ply/fiber waviness is a fiber deviation from a straight alignment in a unidirectional laminate (Thor, et al. (2020)).

On the production of wind turbine blades, geometric changes on tooling surfaces, operator errors and skewed fibres are regarded as factors leading to wrinkles (Galappaththi, et al. (2013)). Wrinkles in composite laminates is a result of various factors, such as temperature gradient during manufacturing of composites structures, the compaction process, component and tool interaction and fibre mismatch in curved portions of the structure (Kulkarni, et al. (2020)). Low inter-laminar shear stress affects the compaction quality of plies in the layup process. As for manufacturing of complex-shaped structures, the low drapability of plies to conform to the required mould design can result in fibre waviness (Hassan, et al. (2017)).

Characteristic parameters of wrinkles are wavelength (λ), amplitude (δ) and a maximum angle (θ_{max}) as shown in Figure 1. Concerning the severity level, there is no consensus on a unique metric. The severity of the defect can be measured by the aspect ratio of the amplitude to wavelength (δ/λ) (Wang, et al. (2012)). Additionally, Maximum angle is often regarded as a critical parameter (Mukhopadhyay, et al. (2015)), having the most significant influence on the mechanical properties of the laminate (Davidson, et al. (2012)). Amplitude-to-thickness ratio (δ/t) is also considered detrimental to assess strategies for fibre waviness (Thor, et al. (2021)). In this work, the aspect ratio of amplitude to half-wavelength ($2\delta/\lambda$) and max. wrinkle angles (θ_{max}) are taken as a metric on the severity level of a given wrinkle as it considers the main geometric parameters of the defect at the cross section.

Manufacturing of artificial wrinkles requires thorough methods as the specimens often undergo variability in the wrinkle parameters. One of the applied methods lies in inserting a plastic rod in the region of interest. The vacuum is then applied to induce a wrinkle at the region where the rod is placed. Afterwards, vacuum is removed to extract the rod and subsequently, vacuum is re-applied to create a resin pocket shaping the wrinkle (Leong, et al. a (2012), Leong, et al. b (2012)). Alternatively, ply strips are placed in the target location where the wrinkle severity is controlled by varying the width and thickness of the inserted strips (Mukhopadhyay, et al. (2015),Riddle III, W.W. (2013)). A different method requires a female metal plate tooling to create the sinusoidal wave configuration intended for the wrinkling (Thor, et al. (2021)). The production method in this work was conceived on reproducing a wind turbine blade (WTB) manufacturing step which can result in out-of-plane wrinkles.

Several methods are employed to represent wrinkles through numerical models (Leong, et al. a (2012), Leong, et al. b (2012), Smith, et al. (2014), Mukhopadhyay, et al. (2015), Bender, et al. (2019), Xie, et al. (2018), Xie, et al. (2015)). Analytical models are equally described in the literature (Hsiao and Daniel a (1996), Hsiao and Daniel b (1996), Zhu, et al. (2015)). Finite element modelling is targeted in this work as it allows detailed representation of geometrical complex features. An idealized finite element model (FEM) based on the characteristic parameters of wrinkles was built with 3D solid elements (Leong, et al. a (2012), Leong, et al. b (2012)). Non-destructive test (NDT) imaging were converted into numerical models by using a MATLAB-based simulator to take ultrasonic data as a material map from laminates with wrinkles and converted into an Abaqus finite element mesh by using a 3D vector field mapping of fibre orientations (Smith, et al. (2014), Xie, et al. (2015)). Trigonometrical functions are frequently used to generate a parameterized model of the defect. Mathematical cosine function controls the through thickness mesh coordinates of a wrinkling configuration built-in Abaqus/Explicit with 3D elements, in which parameters are measured directly from test coupons (Mukhopadhyay, et al. (2015)). In a similar approach, sine function was taken to control the mesh nodes of a 3D solid model introducing a parameter to control the flattening of the wrinkle, so named wash out degree (Bender, et al. (2019)). Multi-directional parametric models based on a Gaussian-modulated cosine-wave profile were applied for the topology definition of wrinkles (Xie, et al. (2018)). In the same work, the MATLAB-based simulator developed by Xie, et al. (2015) is used to search the best Gaussian-envelope cosine-shape fit to the image of the wrinkle coupon specimens. Although the transfer process allows the selection of uniform and ply-thickness dependence of fibre volume fraction (FVF), the authors conduct the analysis with constant FVF arguing for a tendency of uniformity in FVF during

the curing process. The numerical method in this work is related to an image based model which extracts the true parameters of the cross section defect image.

Reduction in laminate stiffness is registered in composite structures with fibre waviness (Chan and Wang (1994), Chan and Chou (1995)). An analytical constitutive model was developed and experimentally verified to predict the elastic properties of unidirectional composites with fibre waviness. It was noticed a decrease of Young´s modulus with increase in fibre waviness, although for crossply laminates the Young´s modulus was not proved to be a sensitive function of fibre waviness (Hsiao and Daniel a (1996)). Experimental tests with wrinkle coupon specimens are often conducted in servo-hydraulic machines with prior buckling stress investigation (Hsiao and Daniel a (1996)). Instrumentation is usually based on high speed cameras and digital image correlation (DIC) for measurement of full 3D displacement and 2D strain on the specimen surface (Mukhopadhyay, et al. (2018), Mukhopadhyay, et al. (2018)). As the aim of this work is to validate a numerical approach for stiffness prediction in laminate with artificial wrinkles, suffice the strain measurement around the target regions by means of extensometers.

Section 2 presents the steps required to develop the methodology of analysis to validate the numerical models proposed in this work. In section 3, the detailed configuration of wrinkles is described along with manufacturing processes. In section 4, the numerical models are presented with a two step-modeling having an image based model used to retrieve the geometry for construction of a finite element model. In section 5 the experimental design is described. The results of stiffness prediction are presented in section 6. Finally, the conclusion of this work is shown in section 7.
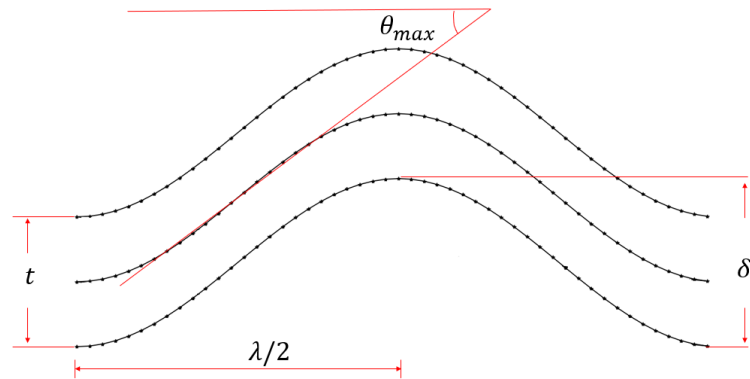
Figure 1. Geometric parameters regarded for severity determination of a wrinkle defect (Mukhopadhyay, et al. (2018)).

2   Methodology of Analysis

The evaluation of wrinkles impact on wind turbine blades (WTB) is planned across five stages: (i) characterization of wrinkles based on geometrical parameters and critical blade operation scenario - this stage is dedicated to replicate wrinkles representative of a wind turbine blade assuming the aspect ratio and max. angle as metric of severity (Figure 1). In this work, a defect

is considered significant for investigation when not identified via current NDT methods and later, without a proper repair, will be exposed to operation with potential effects on the structural performance of the blade. That case occurs when the defect is small in amplitude and is located in the subsurface of a thick stack/layup region of the blade. (ii) Manufacturing of artificial wrinkles by replicating a manufacturing process that potentially lead to wrinkles in wind turbine blades structures - at this stage two types of wrinkles configurations are introduced. (iii) Image processing to capture the geometrical parameters of the true defect - in this stage the wrinkle cross-section image of the coupon specimen is analysed by Matlab-scripted algorithms for the image treatment and retrieval of each individual wrinkling ply contour. (iv) FE modelling of the physical defect is conducted in this stage, in which the geometrical parameters for the individual ply contours from the stage (iii) are applied to support the geometry construction of the defect in an Abaqus FEM. (v) FEM validation is conducted in this phase based on the results obtained in the experimental campaign for a quasi-static loading. The same boundary conditions and load amplitude applied during the test campaign are reproduced in the FEM in order to verify the correlation of the results. Figure 2 presents the schematic of the methodology stages.
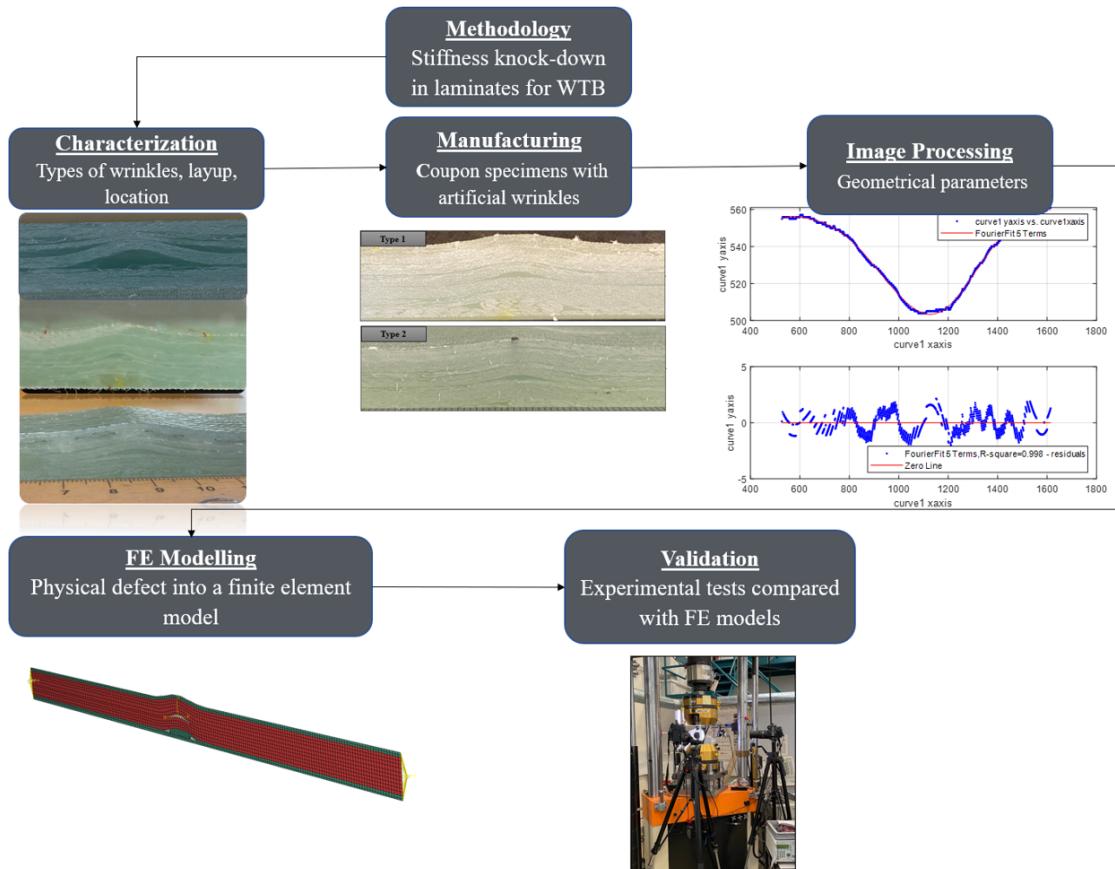
Figure 2. Schematic of the steps used to carry on the methodology of analysis to evaluate the stiffness knock-down of laminates for WTB.

3   Artificial Wrinkle Manufacture

3.1   Configuration of Wrinkles

Post manufacturing evaluation of blade structural integrity is conducted via visual inspection and NDT methods to monitor quality conformity with standards requirements. Presently, NDT technologies applied to large structures such as wind turbine blades lack precision to identify wrinkles defects below the laminate. As a consequence, non detected wrinkles defects can remain in the blade without repair during operation, which can potentially lead to failure. Wrinkle defects can appear in different forms during the manufacturing process, in which significant variables such as the angle defining the deviation in the fibre direction, the number of plies through thickness and the symmetry/asymmetry of the defect can change from one wrinkle to the other (Xie, et al. (2018)). The root section is prone to a surge of wrinkles due to pronounced curved shapes, which can result in fold regions during the blade hand layup and due to relative thick laminate sections. Therefore, the characteristic wrinkles evaluated in this work follow the same manufacturing step, which can lead to such defects. In this work, two types of wrinkles configurations are selected for analysis as shown in Fig. 3. The selection is defined based on wrinkles considered sufficiently small to be identified during the inspection. The geometrical parameters are specified in Table1. Both types of wrinkles are designed with the same amplitude, but different aspect ratios and maximum angle. What is referred to as the aspect ratio is the ratio of wrinkle amplitude to half-wavelength. The higher the aspect ratio, the more severe the wrinkle configuration will be as that will lead to larger angles. The maximum angle is determined based on amplitude, δ, and wavelength, λ, as in Eq.1 (Bender, et al. (2019), Adams and Hyer (1993)). The defects are manufactured under controlled conditions, so the ply of maximum angle is located at the center of the specimen. The layup is shown in Fig. 3, in which UD layers are placed amidst biax plies. A biax ply with a local fold is placed on the bottom of the layup in order to reproduce one of the production processes, which can lead to wrinkles. That way, both types of wrinkle specimen is embedded with two shapes of waviness: a symmetric one positioned at the center of the layup and a second asymmetric one placed on the bottom of the laminate. A common characteristic of asymmetric wrinkles, also known as s-shaped, is the presence of resin zones at either side of the wrinkling as the first wrinkled ply is folded under consolidation pressure (Bloom, et al. (2013)). However, this type of configuration mitigate the accumulation of resin pocket underneath the wrinkle of maximum amplitude, as the effect of the s-shaped wrinkle propagates up to the resin pocket formation. The choice for this wrinkle configuration was selected after experimental test trials proved this configuration with higher strength compared to a wrinkle characterized by resin pocket accumulation. In addition to that, the specimens are manufactured in such a way as to maintain the geometrical parameters and their repeatability. The manufacturing procedure is presented in Section 3.2.

$$\theta_{max} = tan^-1(\frac{\pi \cdot (\delta)}{\lambda}) \tag{1}$$

Table 1. Geometrical parameters for wrinkles configurations type 1 and type 2.

Geometrical Parameters		
	Type 1	Type 2
Aspect Ratio [amplitude/half-wavelength]	1/5	1/10
Amplitude [mm]	2	2
Max. Angle [°]	17.44	8.93

(a) (b)
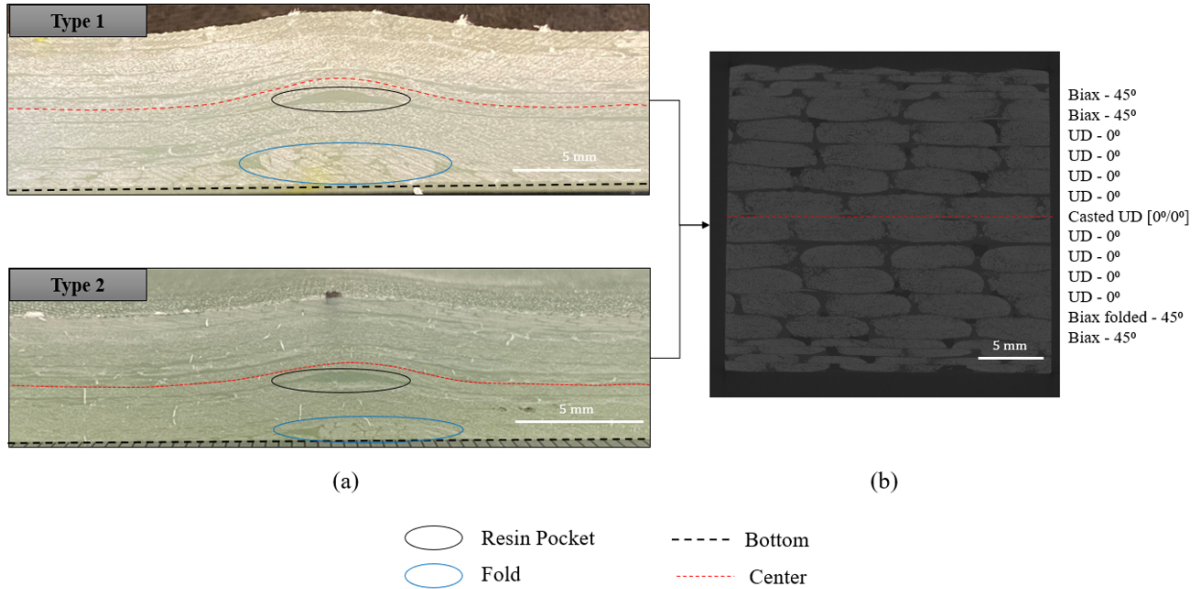
Figure 3. (a) Types of wrinkle configurations selected for the analysis; (b) Layup specification for the transverse cross section of the specimens taken at the flat region which is similar for both wrinkle types.

3.2 Manufacturing of Coupon Specimens

Coupon specimens are produced through two process phases with face sheets of glass fibre reinforced polymer (GFRP) consisting of uni-directional (UD), bi-directional (Biax) and resin epoxy. The UD ply thickness is 0.859 mm, whereas the Biax ply has 0.564 mm. Material properties are presented in Table 2. The transverse contraction values have a neglected influence on the actual longitudinal stiffness of the model. In principle E_{33} should be slightly lower than E_{22} due to the present of secondary oriented backing bundles in the x_2 direction, and accordingly the G_{13} compared to G_{12}. Nevertheless, those values are considered to have a negligible influence on the axial stiffness prediction which is dominated by the E_{11} and G_{12} components. In the first phase UD plies are laid on a mould to form a [0/0] panel. Two UD sheets are stacked together on top of an Aluminium cast mold with geometrical topology equivalent to the wrinkles type 1 and type 2 as defined in Table 1. The artificial defect is induced transversely to the orientation of the fibers along the panel width (Figure 4). Epoxy Hexion resin system with mixing

ratio of 100/28 by weight is used in the infusion. The double UD sheets are impregnated with resin through a vacuum-assisted resin infusion (VARI) process. A curing profile of 12 h at $40\,°C$ and 10 h at $80\,°C$ is applied. In the second phase assembling

130 of the coupon specimens is performed as shown in Figure 4. The hand layup follows the sequence $[+45/-45/0/0/0/0/0]_s$, in which the casted UD plies from phase 1 are placed at the center about the symmetry axis of the sample. The second biaxial layer is folded in a direction transversely to the fibre orientation during the layup. The fold is positioned so that is aligned with the center of maximum wrinkle amplitude. The laminate assembly is infused via VARI with the same mixing ratio and curing cycle applied in the first phase of production. The panels produced in phases 1 and 2 undergo visual inspection during resin

135 infusion and post-cure to assure quality checking for dry spots and voids. Subsequently, the specimens are evenly sliced in dimensions of 400x25x11 mm for both configurations.
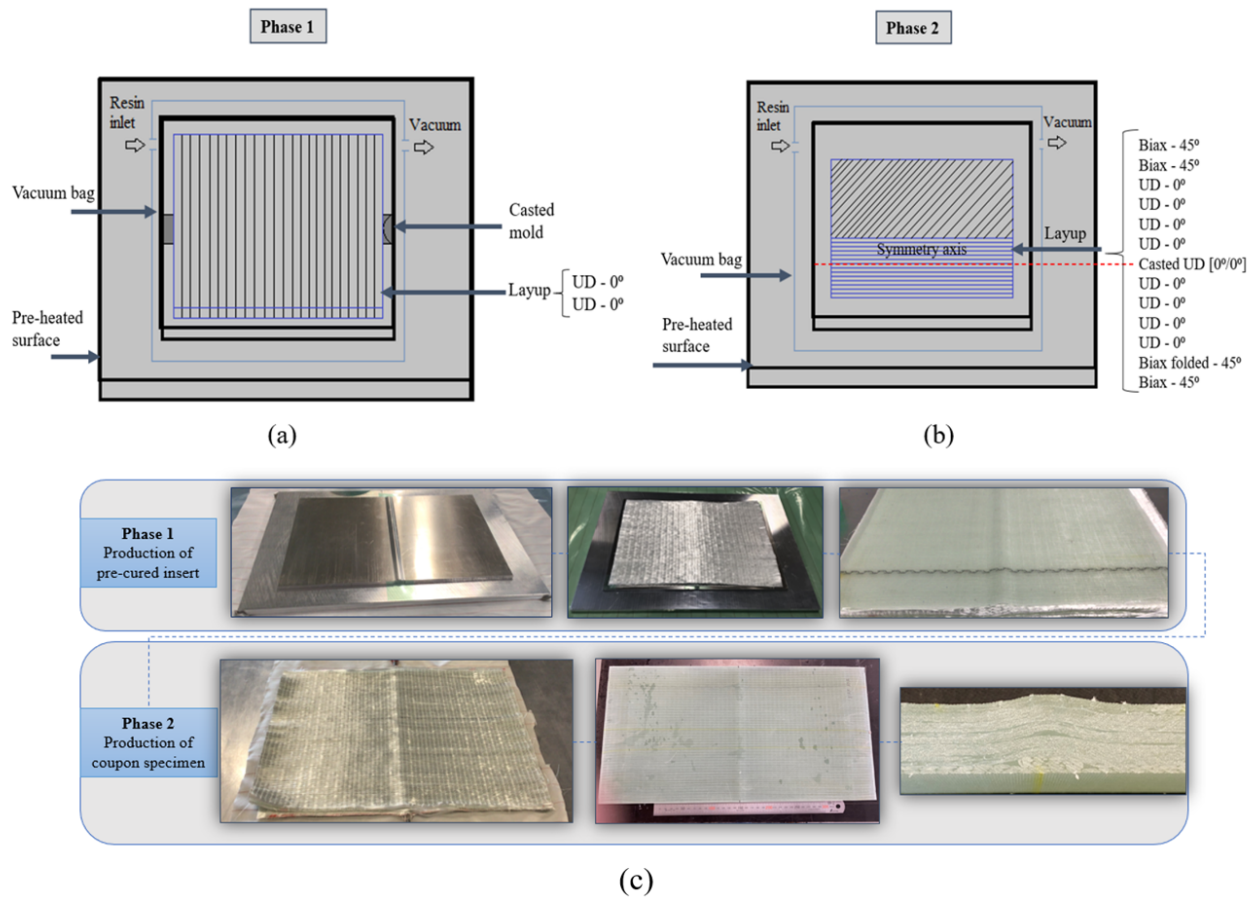
Figure 4. Production phases for the artificial wrinkle defect: (a) schematics of production table for phase 1 with VARI of double UD plies resulting in a pre-cured insert for phase 2. (b) schematics of the VARI in phase 2 in which the complete laminate is assembled with the pre-cured insert from phase 1 leading to the coupon specimen. (c) Image fluxogram indicating the production steps in phase 1 and phase 2.

The main advantages of the two phases technique are the control over the required geometric parameters and mitigation of the resin pocket around the wrinkle of maximum amplitude, resultant from the fold effect in the Biax layer. On that basis, the artificial defect is manufactured in a way to hold a close approximation of a characteristic defect of a WTB.

Table 2. Elastic properties for the GFRP and epoxy material.

	Elastic Properties								
	E_{11} (GPa)	E_{22} (GPa)	E_{33} (GPa)	G_{12} (GPa)	G_{13} (GPa)	G_{23} (GPa)	ν_{12}	ν_{13}	ν_{23}
UD	42.70	12.58	12.58	4.61	4.61	4.61	0.257	0.257	0.364
Biax [+45/-45]	13.92	13.92	13.92	11.5	11.5	5.53	0.533	0.533	0.257
Epoxy	3.2			1.2			0.3		

4 Numerical Modelling

4.1 Image Based Geometric Model

Cross section images of the artificial defect are processed through Matlab-based scripted algorithms. The image processing scheme is performed in a five-step sequence (Figure 5) covering the steps of image processing, filtering, segmentation, fitting techniques for capturing the proper contour of an individual fiber and a 2D coordinate map generated to support the finite element modeling. A combination of the image processing toolbox available on Matlab with a series of encoded scripts are used for the image processing, filtering, segmentation and fitting of each individual fiber. The filtering technique of the wrinkle image is based on rank filtering /median filtering, which removes outliers without reducing the resolution of the image. When it comes to the fitting technique, each individual fiber is evaluated accordingly to the least residuals method.

Image threshold isolating a range of pixels contours from the fibres is conducted in the first step. The second step executes a series of commands to segment the target contours after filtering outliers. In the third step, fitting techniques are used in order to approximate each individual contour to a mathematical model. Various fitting types are tested individually in the fibre contours. The fitting technique elected for an individual fibre contour is based on the least residuals method. As such, that step generates contours with equally spaced points to support the mesh generation of the FEM. In the fourth step 2D coordinates are extracted from the fitted contours. The map of coordinates is stored as an input file used to create splines of the wrinkling section. At the last step the coordinates are used to generate the splines to support the geometry construction of the FEM into ABAQUS.

For each defect configuration, two types of finite element models are derived: a surrogate model and a high fidelity model. The surrogate model solely accounts for the effect of individual ply waviness disregarding the effect of complexity geometry resultant from the fold in the Biax ply and resin regions. The high fidelity model regards the effects of resin regions and asymmetric wrinkle shapes resultant from the s-shaped Biax layer. The detailed finite element model is presented in Section 4.2.
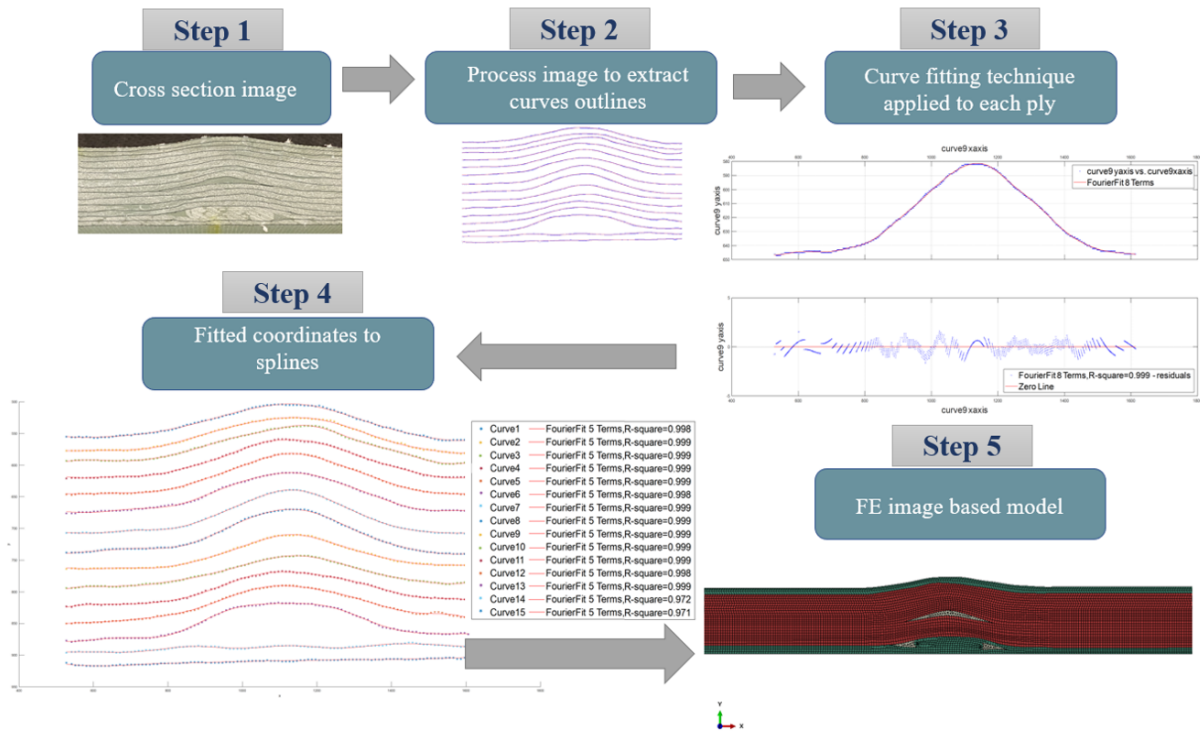
Figure 5. Four-step sequence to translate the cross section defect profile into a finite element model by thresholding individual contours, segmentation of such contours and outliers removal, mathematical fitting techniques to generate even spaced coordinates and finally the extraction of 2D coordinates to import into ABAQUS.

4.2   Finite Element Model

The numerical simulations are conducted in ABAQUS standard version 2021, meaning that an implicit linear Newton Raphson solver is used to predict the model response. Two 2D models are obtained with geometrical parameters from the image based geometric model described in section 4.1: a surrogate model (SM) and high fidelity model (HFM) as shown in Figure 6.

The HFM embodies the geometric complexities of the characteristic defect. Thus, the HFM refers alone to high fidelity geometric features represented in the numerical model.Both models (SM and HFM) present approximate the same degrees of freedom, which result in a similar calculation time performed within few minutes on a 16 CPUs Linux cluster. 2D 8-node plane stress elements with biquadratic reduced integration (CPS8R) are used to discretize the specimen geometry. However, in the HFM the resin regions are represented by 6-node modified plane stress elements with hourglass control (CPS6M) as triangular elements enable mesh refinement with acceptable resolution within the region. The SM contain the same elements used in the HFM excepting the modified plane stress elements for the resin region, which is not represented. The characteristic element

length is defined based on mesh convergence studies tracking the displacement values at the regions of interest. Such regions are the locations where the extensometers are placed in the test campaign as described in section 5.

175 Selected nodes at 25 mm away from the wrinkle center are used to track displacement values around the wrinkle section. The displacement in the flat section is tracked by selected nodes at 40 mm and 65 mm from the center. During the mesh sensitivity analysis, the displacement is plotted over the mesh size. The mesh sensitivity studies show convergence for a characteristic element length of 0.4 mm. The model is built in a ply-by-ply scheme, meaning that each layer is discretized individually as shown in Figure 7.
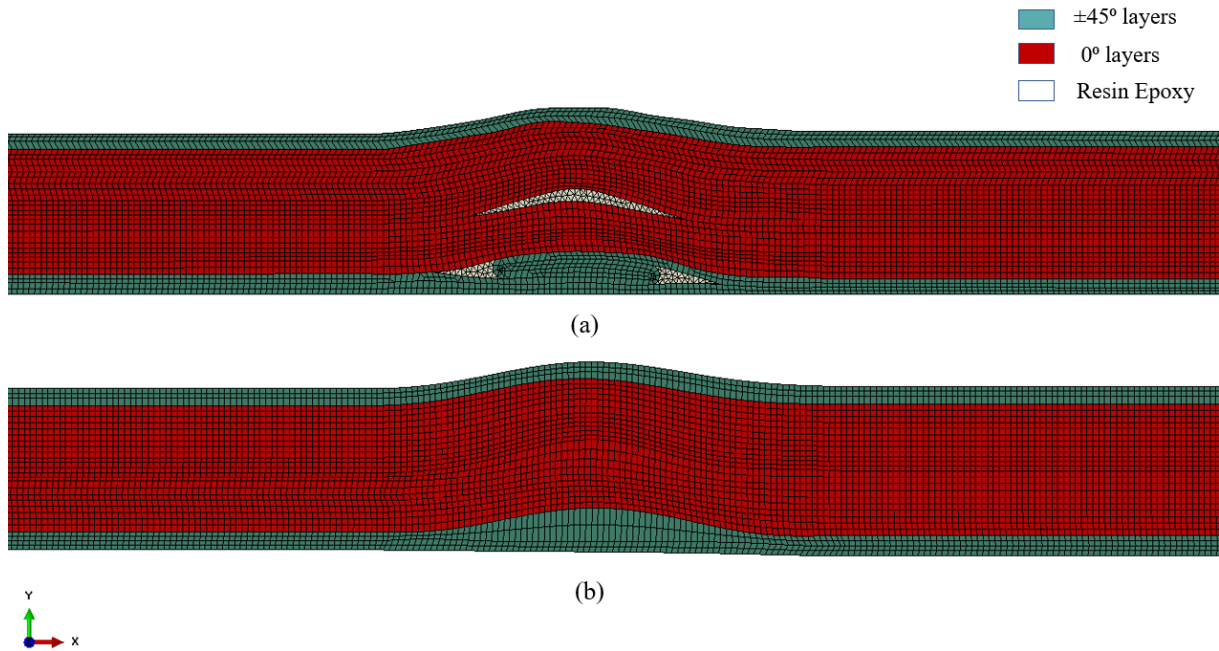
Figure 6. Comparison of mesh discretization with the geometric details of the wrinkle type 1 for the models: (a) HFM present the geometrical complexities of a fold wrinkle and resin pocket (b) SM present a simplified geometrical configuration.

180 The local material orientation is assigned accordingly with the upper contour of each ply. Directions 1 and 2 are the global x and y directions, respectively. Constraints are introduced through kinematic couplings at reference points located sufficiently close to the model ends to avoid unwanted bending moments. The degrees of freedom of the reference point on the left end of the model are restrained in the x- and y-directions. The load is applied to a reference point on the right end of the model. The reference point serves as a master node transferring the loading via the kinematic coupled constraints (all degrees of freedom

185 are constraint) to the slave nodes on the neighbour surfaces at each end of the model. In consequence, the slave nodes are constrained to the rigid body motion of the master node.

Load frequency and amplitude are applied to the model according to the performed experimental tests. The node sets recording the displacements are defined in the same position that the extensometers are placed during testing in order to track the displacement at the same location, for a straightforward comparison. The reference point at the left end of the model (also used to constraint the DOFs) is also used to track the reaction load.
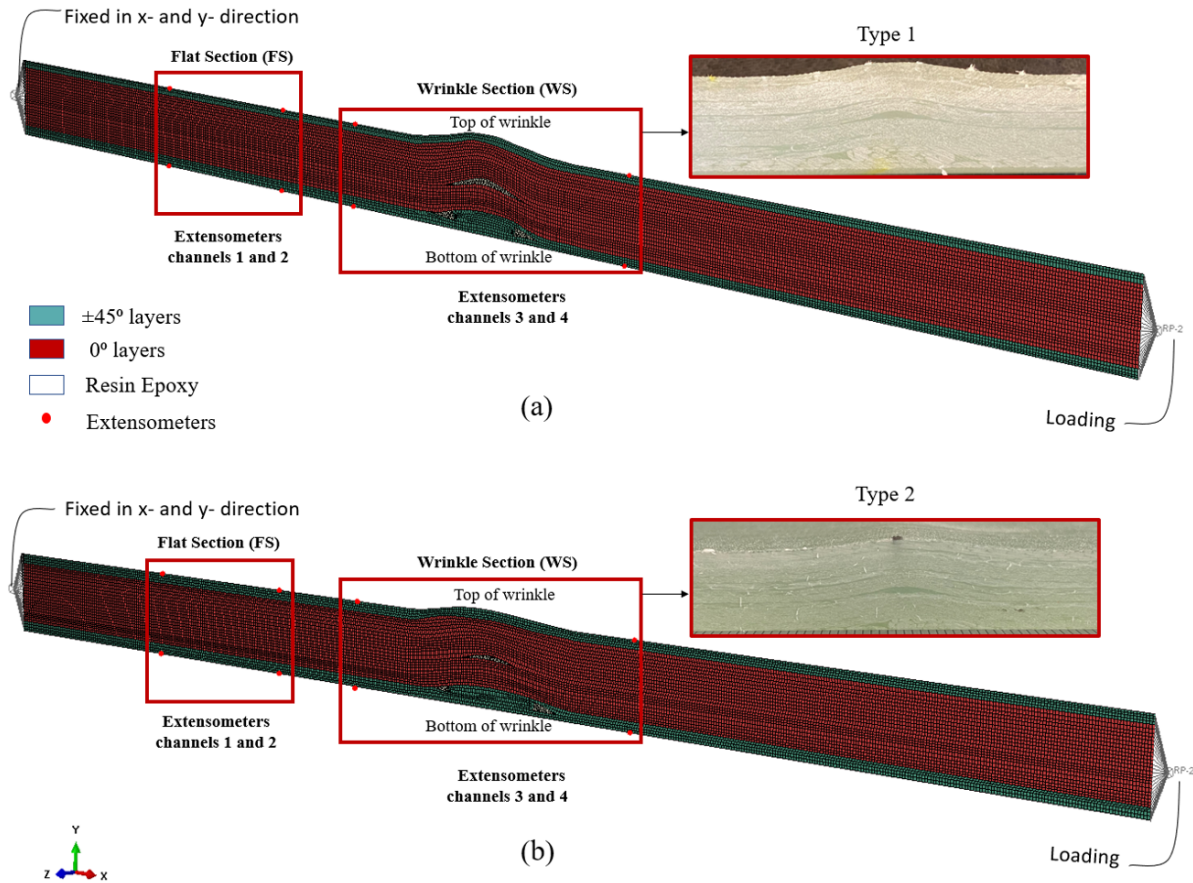
Figure 7. High fidelity finite element model modelled in a ply-by-ply sequence, with biaxial layers on top and bottom, UD layers in between and resin pocket around the biax fold and underneath the ply contour of max. amplitude : (a) coupon specimen model for wrinkle type 1 (b) coupon specimen model for wrinkle type 2.

5 Experimental tests

Two specimens of each configuration type 1 and type 2 were tested under quasi-static loading with a servo-hydraulic tensile test machine Instron 8533, with load cell UK 084 and 250 ± 1.20 kN capacity. The specimens were mounted into grips with 50 mm gauge length extensometers, aligned back to back with the wrinkle in the center. For the flat section extensometers of

195 25 mm gauge length were positioned at a distance of 40 mm away from the wrinkle center. High-speed cameras were used to capture images of the side and back views of the gauge section as shown in Figure 8. The images from the camera are not relevant at this study as the samples are not driven to failure. In an upcoming study where the samples are tested under reverse fatigue the images are explored displaying the location for delamination initiation.
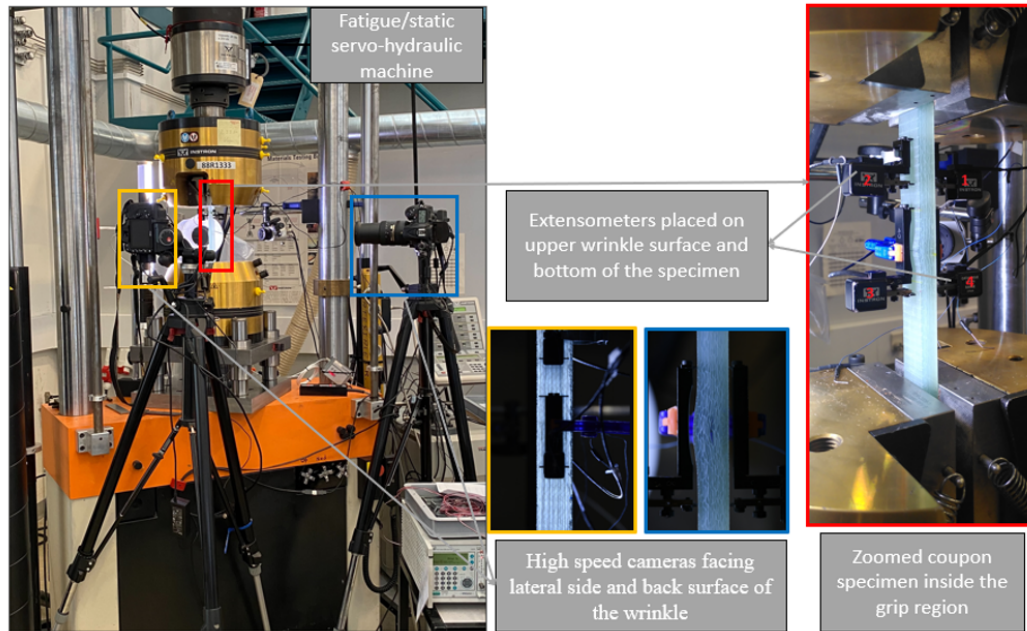
Figure 8. Experimental setup with the specification of devices used for test and acquisition of results, with the positioning of coupon specimen in the test rig and placement of acquisition channels around the gauge section.

Prior to testing, the specimens were polished with sandpaper and treated with a lacquer Acryl spray to increase the bonding
200 strength and attenuate the effect of rough side borders (Yang, et al. (2019)). A numerical buckling analysis was conducted to verify that the sample length within the grip section was bellow the buckling limit under compression for the target load. A strain rate of 0.01 %/s was used for three elapsed cycles. As a loading, a tension-compression test with load amplitudes of $\pm$ 16 KN was applied over an external controlled program, which feeds the machine with a triangular ramp loading. According to the ISO and ASTM standard, the stiffness should be taken over a strain range of 0.2% (Iso E. 527-1. (2012), ASTM D3039.
205 (2017)). The load level is chosen such that the deformation exceeds this range but still stay bellow load-levels where damage initiation could be introduced. The tensile-compression strain was measured at the four channels of the clip gauge extensometer.

6   Results and Discussion

In this study, the stiffness is described as the overall slope of the stress versus strain relation. Thereby, stiffness values obtained from the experimental tests are measured of the slope load versus strain shown in Figure 9 and averaged by the mean cross-sectional area of the flat section for the two sets of specimens tested. As the wrinkle out of the straightness path results in a bending around the center of symmetry, strain results from the top and bottom of the wrinkle were averaged to account for the eccentricity effect. To preserve the correlation, the strain results from the top and bottom at the flat section were equally averaged. Figure 9 shows the hysteresis loop in detail for both types of wrinkle configurations and sections.

The hysteresis loss observed experimentally is mainly driven by the viscoelastic behaviour of the polymer matrix. Although not considered in the present numerical model, the viscoelastic effect can be addressed by using a visco-material law. The damping is calculated by averaging the hysteresis loop area over the three reversal cycles. The wrinkle section experience higher energy losses as the in-plane shear effect leads to higher damping when compared to the flat section. The Type 1 specimen, which has a higher maximum angle has also a higher damping effect in regards to type 2. Experimental damping values are shown in Table 3. The damping from the wrinkle section is approximately three times higher compared with the damping observed in the flat section. By comparing both configurations, the damping of type 1 wrinkle is 32% higher than type 2. Consequently, the higher the wrinkle angle, the higher the energy losses as a result of the shear loading of the resin in the wrinkle section.

Figure 10 shows the experimental results for stiffness in both types of specimens at the wrinkle section and flat section against the predictions pointed by the surrogate model and the high fidelity model along with respective average deviation. The error bars show the actual stiffness values measured for the two samples tested of each type of wrinkle. The numerical models are verified through correlations of FE simulations and the results from experimental tests. When it comes to experimental data, the stiffness at the flat section has a minor deviation comparing type 1 and type 2 configurations as the samples might deviate in fiber volume fraction or potential microcracks that can arise during the manufacturing process. When the deviation is observed in the numerical results, that is in principal due to a slight difference in thickness for each type of wrinkle which was taking into account in the model for both types of samples. Furthermore, the complexity of the geometrical features present in the HFM induce a different pattern of mesh where the local size of few elements are different from the SM which is simpler and therefore straightforward for a even sized mesh.

The stress vs per cent strain of coupon specimens shown in Figure 11 are obtained from averaging the extensometers results at the top and bottom of the wrinkle located in a gauge length of 50 mm around the center. The strain levels are also measured at the flat section, 40 mm away from the wrinkle center with an extensometer gauge length of 25mm. The results obtained from the numerical models are extracted at the same position as the experiments. wrinkles are introducing an asymmetry in the experimental setup. The difference in stiffness in tensile and compression side will depend on the asymmetry if the test-geometry introduced by the winkle and thus on details on how the samples are clamped and alignment of the pistons. Therefore we are mainly focused on averaging the stiffness at the two sides what is done subsequently in the comparison.
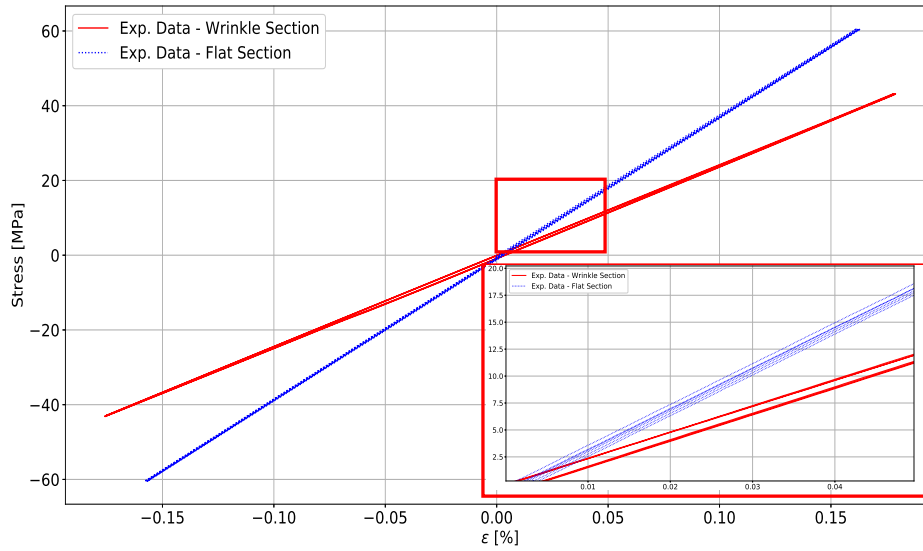
(a) Wrinkle type 1
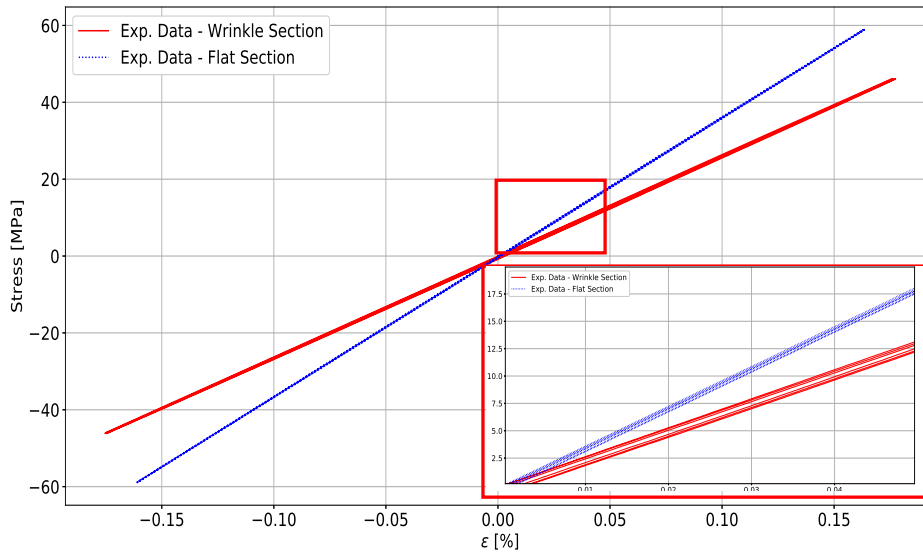
(b) Wrinkle type 2

Figure 9. Stress vs. strain graph of wrinkle specimens type 1(a) and type 2(b) with average strain between top and bottom. The strain is measured over 50 mm around the wrinkle section and 25 mm around the flat section (see Figures 7 and 8) with local zoom showing the hysteresis loop of the elapsed cycles.
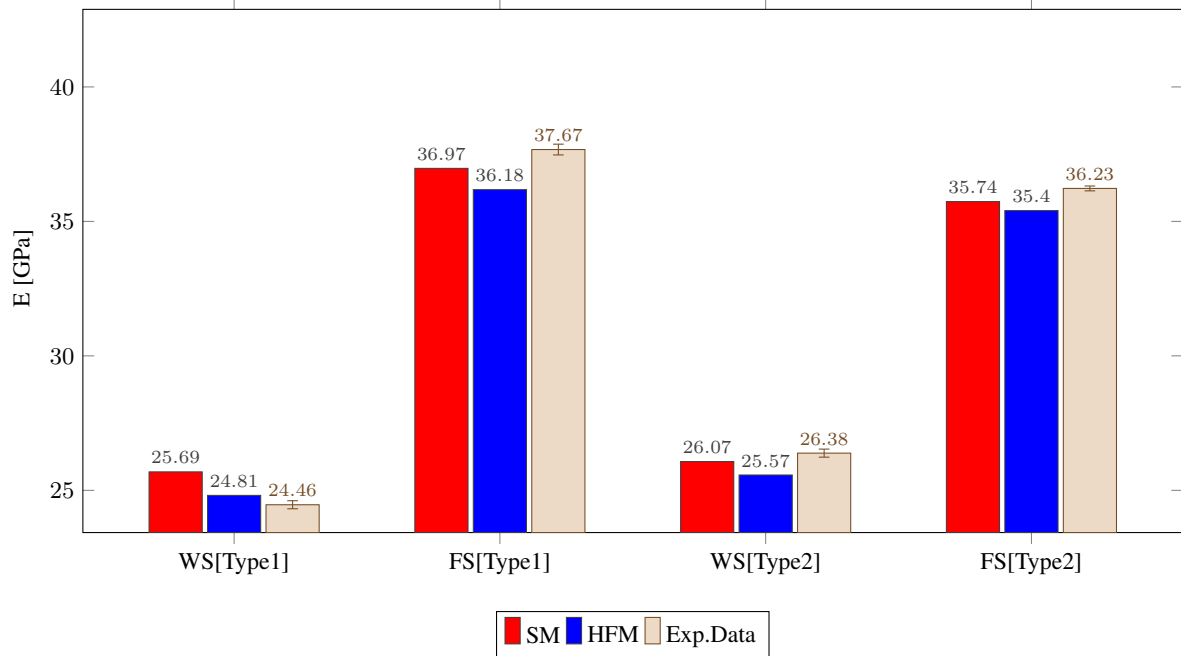
Figure 10. Stiffness results for wrinkles type 1 and type 2 around the wrinkle section (WS) and the flat section (FS) based on the numerical model predictions and experimental data.

Table 3. Experimental Damping values for specimens type 1 and type 2.

	Exp. Results Damping[-]	
Specimen	Flat Section	Wrinkle Section
Type 1	0.021	0.066
Type 2	0.018	0.050

The knock-down in stiffness for wrinkle type 1 is 54%, whereas for wrinkle type 2 is 37%. Consequently, the metric applied for wrinkle severity is in conformity to the results observed as wrinkle type 1 is proven to be the most severe. The stiffness knock-down observed in the high fidelity model is 46% for wrinkle type 1 and 38% for wrinkle type 2. The model prediction for the wrinkle section type 1 has a difference of 1.4% in stiffness against the test results for the high fidelity model, while in type 2 this difference is 3.2%. Thus, the modelling of fold complex pattern and resin regions is relevant for accurate prediction of the component structural stiffness. However, the narrow deviation from the surrogate model compared to test results suggest that the effect of fiber waviness through thickness is more critical to the stiffness knock-down than the local effect of the fold or light concentrations of resin regions. At the flat section is observed a deviation of 4.1% from the high fidelity model compared to experimental results in type 1 specimen, while type 2 this deviation is of 2.3%. This difference can be perceived by the simplification in modelling for the flat section.
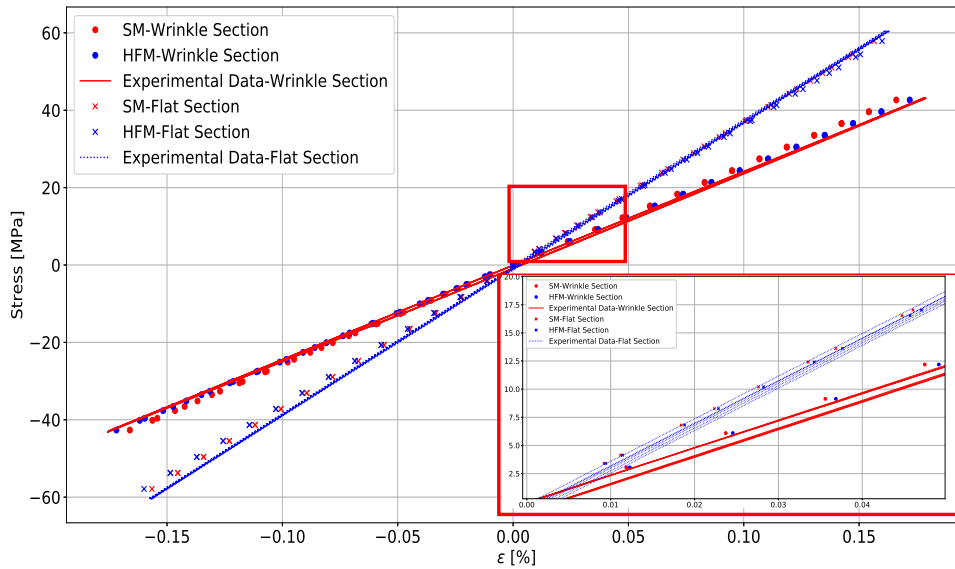
(a) Wrinkle type 1
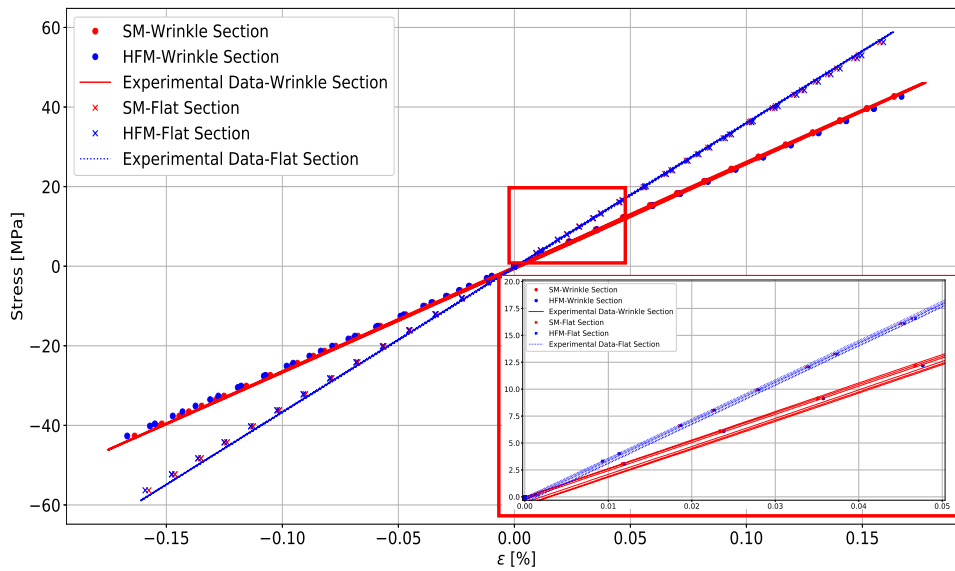
(b) Wrinkle type 2

Figure 11. Prediction of numerical model results against experimental tests for coupon specimens with two configurations of wrinkles.

As the precise representation of the wrinkle section was the primary concern, outside that region the plies were represented as straight lines extended by the ends of each individual wrinkling ply. Furthermore, the fiber volume fraction in both models was considered constant, which implies in potential deviation of stiffness prediction on the FE model. For future work in which fatigue loading situation will be considered, the variation in fiber volume fraction shall be accounted as the slight difference in stiffness plays an important role in crack-onset and delamination path. Moreover, accounting for resin regions is equally relevant in fatigue loading as the thermo-viscoelastic effect of the resin can lead to a pronounced damping effect.

7 Conclusions

In this study, a methodology to manufacture, to test and to predict the stiffness knock-down in laminates with artificial wrinkles representative for wind turbine blades is verified through numerical models and experimental tests. As wrinkles are prone to form during the manufacturing process of blades, it is fundamental to draw a method allowing to evaluate the impact of such defects with respect to the structural performance. An element test procedure representing laminates with characteristic wrinkles as typically occurring in wind turbine blades is presented for verification purpose of numerical models. The characteristic laminates were investigated experimentally and numerically under quasi-static loading situation. Each ply waviness was modelled individually with geometrical parameters represented as the physical defect. Experimental tests were used to verify the FE-models accounting for the complex geometrical effects compared to FE-models representing only the true fiber wrinkling region. Two configurations of wrinkles were accounted, where the critical parameters are defined by the aspect ratio of amplitude to half-wavelength along with the max. angle. The most severe wrinkle, type1, of higher aspect ratio and higher max. angle experienced a knock-down of 54% in stiffness compared to 37% for the wrinkle type2. The models presented a fair correlation with the stiffness observed in the experimental tests. Although the geometrical effects of Biax fold and resin regions was prove to not significantly influence the knock-down in stiffness for the quasi-static case. Under fatigue loading the geometrical deviations could be detrimental as it decreases the load carrying capacity of the laminate. Future work shall take into account the effect of variation in fiber volume fraction accounting for the validity of the model tested for fatigue loads and effect of surrounding structure in a full blade.

Author Contributions

HGM developed the research methods, elaborated the computational scripts and FE numerical models, analyzed the data, prepared the figures, and was lead author of the article. LPM assisted in the conceptualization, supervision of data analysis, supervision of numerical modelling and test results providing extensive feedback over the various reviews. FM, JB, PUH, KB and XC provided technical supervision and thorough review of the work methodology and reviewing the writing.

Competing Interests

The contact authors have declared that neither they nor their co-authors have any competing interests.

Data Availability

280   All results data are published as line and bar plots in the paper.

Acknowledgements

The authors acknowledge the support from the Danish Energy Agency through the EUDP grant 64018-0068 in the ReliaBlade project.

References

285

Kulkarni, P., Mali, K.D. and Singh, S.:An overview of the formation of fibre waviness and its effect on the mechanical performance of fibre reinforced polymer composites. Composites Part A: Applied Science and Manufacturing, 137, p.106013, https://doi.org/10.1016/j.compositesa.2020.106013, 2020.

Hassan, M.H., Othman, A.R. and Kamaruddin, S., 2017. A review on the manufacturing defects of complex-shaped laminate

290   in aircraft composite structures. The International Journal of Advanced Manufacturing Technology, 91(9), pp.4081-4094.https://doi.org/10.1007/s00170-017-0096-5, 2017.

Galappaththi, U.I.K., De Silva, A.M., Draskovic, M. and Macdonald, M., 2013, March. Strategic quality control measures to reduce defects in composite wind turbine blades. In International Conference on Renewable Energies and Power Quality (ICREPQ'13), Bilbao (Spain) (pp. 20-22).

295   Wang, J., Potter, K.D., Hazra, K. and Wisnom, M.R., 2012. Experimental fabrication and characterization of out-of-plane fiber waviness in continuous fiber-reinforced composites. Journal of Composite Materials, 46(17), pp.2041-2053,https://doi.org/10.1177/0021998311429877, 2012.

Davidson, P., Waas, A., Yerramalli, C.S., Chandraseker, K. and Faidi, W., 2012. Effect of fiber waviness on the compressive strength of unidirectional carbon composites. In 53rd AIAA/ASME/ASCE/AHS/ASC Structures, Structural Dynamics and

300   Materials Conference 20th AIAA/ASME/AHS Adaptive Structures Conference 14th AIAA (p. 1422),https://doi.org/10.2514/6.2012-1422, 2012.

Mukhopadhyay, S., Jones, M.I. and Hallett, S.R., 2015. Compressive failure of laminates containing an embedded wrinkle; experimental and numerical study. Composites Part A: Applied Science and Manufacturing, 73, pp.132-142, https://doi.org/10.1016/j.compositesa.2015.03.0122, 2015.

305   Thor, M., Mandel, U., Nagler, M., Maier, F., Tauchner, J., Sause, M.G. and Hinterhölzl, R.M., 2021. Numerical and experimental investigation of out-of-plane fiber waviness on the mechanical properties of composite materials. International Journal of Material Forming, 14(1), pp.19-37,https://doi.org/10.1007/s12289-020-01540-5, 2021.

Wang, L., 2001. Effects of in-plane fiber waviness on the static and fatigue strength of fiberglass (Doctoral dissertation, Montana State University-Bozeman, College of Engineering).

310   Lightfoot, J.S., Wisnom, M.R. and Potter, K., 2013. Defects in woven preforms: Formation mechanisms and the effects of laminate design and layup protocol. Composites Part A: Applied Science and Manufacturing, 51, pp.99-107,https://doi.org/10.1016/j.compositesa.2013.04.004, 2013.

Leong, M., Overgaard, L.C., Thomsen, O.T., Lund, E. and Daniel, I.M., 2012. Investigation of failure mechanisms in GFRP sandwich structures with face sheet wrinkle defects used for wind turbine blades. Composite structures, 94(2),
315   pp.768-778,https://doi.org/10.1016/j.compstruct.2011.09.012, 2012.

Leong, M., Hvejsel, C.F., Thomsen, O.T., Lund, E. and Daniel, I.M., 2012. Fatigue failure of sandwich beams with face sheet wrinkle defects. Composites science and technology, 72(13), pp.1539-1547,https://doi.org/10.1016/j.compscitech.2012.06.001, 2012.

Riddle III, W.W., 2013. Development of reliability program for risk assessment of composite structures treating defects as
320   uncertainty variables. Montana State University.

Smith, R.A., Xie, N., Nelson, L.J. and Hallett, S.R., 2014, October. Modelling the mechanical properties of as-manufactured composite components based on 3D non-destructive characterisation. In Proc. European Conf. on NDT,

Xie, N., Smith, R.A., Mukhopadhyay, S. and Hallett, S.R., 2015, July. Modelling the mechanical properties of wrinkled composites from NDT data. In Proceedings of the 20th International Conference on Composite Materials, Copenhagen,
325   Denmark (pp. 19-24).

Bender, J.J., Hallett, S.R. and Lindgaard, E., 2019. Parametric study of the effect of wrinkle features on the strength of a tapered wind turbine blade sub-structure. Composite Structures, 218, pp.120-129,https://doi.org/10.1016/j.compstruct.2019.02.0651, 2019.

Xie, N., Smith, R.A., Mukhopadhyay, S. and Hallett, S.R., 2018. A numerical study on the influence of composite wrinkle
330   defect geometry on compressive strength. Materials & Design, 140, pp.7-20,https://doi.org/10.1016/j.matdes.2017.11.034, 2018.

Chan, W.S. and Wang, J.S., 1994. Influence of fiber waviness on the structural response of composite laminates. Journal of Thermoplastic Composite Materials, 7(3), pp.243-260.

Chan, W.S. and Chou, C.J., 1995. Effects of delamination and ply fiber waviness on effective axial and bending stiffnesses in composite laminates. Composite structures, 30(3), pp.299-306,https://doi.org/10.1177/089270579400700306, 1995.

Hsiao, H.M. and Daniel, I.M., 1996. Elastic properties of composites with fiber waviness. Composites Part A: Applied Science and Manufacturing, 27(10), pp.931-941,https://doi.org/10.1016/1359-835X(96)00034-6, 1996.

Mukhopadhyay, S., Nixon-Pearson, O.J. and Hallett, S.R., 2018. An experimental and numerical study on fatigue damage development in laminates containing embedded wrinkle defects. International Journal of Fatigue, 107, pp.1-12,https://doi.org/10.1016/j.ijfatigue.2017.10.008, 2018.

Bloom, L.D., Wang, J. and Potter, K.D., 2013. Damage progression and defect sensitivity: an experimental study of representative wrinkles in tension. Composites Part B: Engineering, 45(1), pp.449-458,https://doi.org/10.1016/j.compositesb.2012.05.021, 2013.

Yang, G., Yang, T., Yuan, W. and Du, Y., 2019. The influence of surface treatment on the tensile properties of carbon fiber-reinforced epoxy composites-bonded joints. Composites Part B: Engineering, 160, pp.446-456,https://doi.org/10.1016/j.compositesb.2018.12.095, 2019.

O'Hare Adams, D. and Hyer, M.W., 1993. Effects of layer waviness on the compression strength of thermoplastic composite laminates. Journal of Reinforced Plastics and Composites, 12(4), pp.414-429,https://doi.org/10.1177/073168449301200404, 1993.

Thor, M., Sauce, M.G. and Hinterhölzl,R.M., 2020. Mechanisms of origin and classification of out-of-plane fiber waviness in composite materials—a review. Journal of Composites Science, 4(3), p.130,https://https://doi.org/10.3390/jcs4030130, 2020.

Hsiao, H.M., Daniel, I.M., 1996. Effect of fiber waviness on stiffness and strength reduction of unidirectional composites under compressive loading. Composite Science and Technology, 56(5), pp.581-593,https://doi.org/10.1016/0266-3538(96)00045-0, 1996.

Zhu, J., Wang, J. and Zu, L.,2015. Influence of out-of-plane ply waviness on elastic properties of composite laminates under uniaxial loading. Composite Structures, 132, pp.440-450,https://doi.org/10.1016/j.compstruct.2015.05.062, 1996.

Iso E. 527-1. Plastics—Determination of tensile properties—Part 1: General principles. International Organization of Standardization: Geneva, Switzerland. 2012.

ASTM AM. ASTM D3039-standard test method for tensile properties of polymer matrix composite materials. Book ASTM D3039-standard test method for tensile properties of polymer matrix composite materials (ASTM International, 2017). 2017.